



Contents lists available at ScienceDirect

# International Journal of Applied Earth Observation and Geoinformation

journal homepage: [www.elsevier.com/locate/jag](http://www.elsevier.com/locate/jag)



## Characterization of an antarctic penguin colony ecosystem using high-resolution UAV hyperspectral imagery

Alejandro Román<sup>a,\*</sup>, Antonio Tovar-Sánchez<sup>a</sup>, Beatriz Fernández-Marín<sup>b</sup>, Gabriel Navarro<sup>a</sup>, Luis Barbero<sup>c</sup>

<sup>a</sup> Institute of Marine Sciences of Andalusia (ICMAN), Spanish National Research Council (CSIC), Department of Ecology and Coastal Management, 11510 Puerto Real, Spain

<sup>b</sup> University of the Basque Country (UPV/EHU), Department of Plant Biology and Ecology, 48940 Leioa, Spain

<sup>c</sup> University of Cádiz, Department of Earth Sciences, International Campus of Excellence in Marine Science (CEIMAR), 11510 Puerto Real, Spain



### ARTICLE INFO

#### Keywords:

Remote sensing  
Antarctic vegetation  
Multispectral  
Drones  
Biological mapping  
Spectral library

### ABSTRACT

Penguin colonies significantly influence the distribution and diversity of vegetation communities in Maritime Antarctica, as they serve as vital sources of nutrients for both terrestrial and aquatic ecosystems. Remote sensing techniques are becoming increasingly common for monitoring these vast Antarctic areas, especially with Unmanned Aerial Vehicles (UAVs) imagery, which provides the highest spatial resolutions to date. In fact, the use of hyperspectral (HS) sensors is crucial for accurately identifying and distinguishing between the main ground characteristics and vegetation communities in an Antarctic penguin colony, making this study one of the first UAV-based HS approaches to our knowledge. Consequently, this study provides a spectral library covering the entire spectral range from 400 to 2500 nm for the five main vegetation communities found at Hannah Point penguin colony (Livingston Island, Antarctica). Through this library, two valuable wavelength regions have been identified for distinguishing these communities based on pigments composition, specifically in the green (495–570 nm) and near-infrared (800–900 nm) ranges, that served as a reference for validating the results using 35 ground reference spectrometry data collected in 1667 wavelength bands within the 320–876 nm range. In addition, the supervised classification approach known as the “Spectral Angle Mapper” has been employed to monitor the coverage of each vegetation community based on the information provided by the aforementioned spectral library. The observed ecological gradient, which reveals an increase in vegetation complexity away from the high-nutrient content guano areas, highlights the influence of guano on the distribution of the main vegetation patterns across the entire penguin colony. The results of this study could serve as a reference point for more sophisticated research involving the use of UAV-based HS or MS sensors in Antarctica, offering unique opportunities to detect small variations in these remote ecosystems resulting from climate change.

### 1. Introduction

A penguin colony constitutes a unique and interconnected ecosystem, mainly composed of guano, vascular plants, coastal algae, lichens, and moss covers (Black, 2016; Huang et al., 2010; Rogers et al., 2020). Guano has been suggested as an important source of bioactive metals (e.g. Cu, Fe, Mn, Zn) to the ocean (Shatova et al., 2016, 2017; Sparaventi et al., 2021), recycling approximately 521 tonnes of Fe per year and thus playing a key role in primary production within the Southern Ocean ecosystem (Belyaev et al., 2023). In addition, guano stains could act as inputs of nutrients in the terrestrial region of marine

Antarctica, influencing the distribution and speciation of vegetation communities (Román et al., 2022; Tovar-Sánchez et al., 2021).

Antarctic vegetation communities have adapted to persist in such extreme environments, with frigid temperatures, elevated UV radiation, limited water availability, and physical isolation acting as main limiting factors (Colesie et al., 2022). However, these communities are especially susceptible to environmental disruptions, and new responses are expected due to the effects of global warming and exposure to direct anthropogenic activities (Atkinson et al., 2019; Colesie et al., 2022). Consequently, local and long-distance dispersal rates are supposed to increase, along with local population size, ultimately reducing the

\* Corresponding author.

E-mail address: [a.roman@csic.es](mailto:a.roman@csic.es) (A. Román).

primary environmental barriers to establishment and colonization, and leading to an increase in biodiversity (Convey, 2011). As a result, the distribution, biomass, and diversity of vegetation communities within an Antarctic penguin colony can be regarded as a direct reflection of their immediate environmental conditions (Convey et al., 2014; Green et al., 2007). These factors may also indicate new trends in penguin populations, as changes in penguin distribution patterns could quickly and indirectly induce changes in vegetation distribution (Atkinson et al., 2019).

Therefore, it is essential to conduct in-depth research to assess the current status and vulnerability of these iconic ecosystems to potential climate change impacts and how these changes may affect vegetation distribution in the future. However, conventional monitoring techniques are arduous and time-consuming, making it difficult not only to reach the colonies due to logistic accessibility aspects but also to work on such vast and sometimes abrupt coasts (Ancel et al., 2017; Brown, 2018; LaRue et al., 2014). Advancements in satellite remote sensing have enhanced monitoring techniques, enabling the detection of changes in penguin abundance (e.g. Barber-Meyer et al., 2007; Lynch & Schwaller, 2014; Mustafa et al., 2017; Pfeifer et al., 2019), and local-scale ecosystem monitoring research (e.g. Brown, 2018; Fretwell & Trathan, 2009, 2020; Fretwell et al., 2015). Despite its larger coverage, data acquisition with satellite remote sensing in maritime Antarctica is challenging due to an almost permanent cloud cover conditions and its coarse spatial resolution (Murray et al., 2010; Pfeifer et al., 2019).

To address the observational gap between accurate but laborious field measurements and large-coverage satellite imagery at relatively coarser spatial resolutions, Unmanned Aerial Vehicles (UAVs) have emerged as a useful tool providing exciting opportunities for the Antarctic ecosystem monitoring (Lucieer et al., 2014; Malenovský et al., 2017). In fact, UAVs provide a non-invasive, frequent, low-cost, and time-efficient alternative to overcome the main limitations of conventional monitoring techniques (Tovar-Sánchez et al., 2021). In the last few years, several studies have used different sensors mounted on UAVs for wildlife monitoring (e.g. Belyaev et al., 2023; Bird et al., 2020; Dunn et al., 2021; Qiao et al., 2023; Wu et al., 2023), to describe vegetated areas (e.g. Lucieer et al., 2014; Miranda et al., 2020; Turner et al., 2018), or to delimit guano stains on penguin colonies by its unique distinctive behaviour in the red and NIR bands (e.g. Firla et al., 2019; Román et al., 2022). The recent development of new hyperspectral (HS) sensors adapted to UAV platforms (Cao et al., 2021) has enhanced the characterization of such heterogeneous ecosystems, combining an unprecedented scale of spectral and spatial resolutions for better discrimination in smaller and sparser areas within the Antarctic ecosystem.

The objective of this work is to assess the spectral separability between the main vegetation features, and the influence of penguin guano on their distribution, through large-scale monitoring using high-resolution UAV HS data, in a case study at Hannah Point penguin colony on Livingston Island (Antarctica). Although previous work has tested UAV-based methodology to monitor vegetation communities (Lucieer et al., 2014; Malenovský et al., 2017; Sotille et al., 2020), the retrieval of more accurate information remains unexplored. The results were validated with ground reference spectrometry data, and then degraded to multispectral imagery for feature identification at a larger coverage. Considering the significant challenge of obtaining this data in such an extreme environment and the ecological role of a penguin colony within the Antarctic ecosystem, this deep analysis sets the base for a more precise interpretation of the changes faced by vegetation communities under the current climate change scenario.

## 2. Material and methods

### 2.1. Study area

Hannah Point ( $62^{\circ}39' S$ ,  $60^{\circ}37' W$ ) is a cramped peninsula located on the southern coast of Livingston Island (South Shetland Islands,

Antarctica) (Fig. 1). It presents a distinctive topography that separates through a steep slope, a sequence of north-northwest cliffs, rising between 30 and 50 m above sea level, from an open beach area (Leppe et al., 2007). In addition, it hosts a diversified fauna, including giant petrels (*Macronectes giganteus*), skuas (*Catharacta* spp.), Weddell seals (*Leptonychotes weddellii*), elephant seals (*Mirounga leonina*), and three different penguin species nesting there: Gentoo (*Pygoscelis papua*), Chinstrap (*Pygoscelis antarcticus*) and Macaroni penguins (*Eudyptes chrysophthalmus*). For this reason, it is one of the frequently visited locations for observing penguins in Antarctica (Barbosa et al., 2013), receiving around 1095 visitors in 2021/22 (IAATO, 2015). The vegetation communities in Hannah Point are characterized by an aggregation of vascular plants mainly consisting of *Deschampsia antarctica* and *Colobanthus quitensis* (Shirihai, 2003), mosses, crustose lichens (e.g. *Caloplaca* s. lat) that typically colonize free of ice rocky areas (Antarctic Treaty Secretariat, 2023), the lichen-forming fungus *Mastodia tessellata* (Fernández-Marín et al., 2019; Garrido-Benavent et al., 2017a; Pérez-Ortega et al., 2010), and the terrestrial algae *Prasiola* spp. forming dense groups in nutrient-rich areas near the guano stains (Atala et al., 2019; Durán et al., 2021; Garrido-Benavent et al., 2017b). In addition, the intertidal shore is characterized by populations of chlorophyte algae (e.g. *Monostroma harriotii*) forming a dense mat on the intertidal rocks, and rhodophyte algae (e.g. *Pyropia endiviifolia*) attached to rocks in the uppermost sea-shore line.

### 2.2. Data collection

To account for the logistical challenges of installing different sensors in the same aircraft within such a dynamically changing meteorological environment, and considering their payload capacity, which serves as the primary limiting factor for carrying heavier sensors, two different UAVs were employed to survey the entire penguin colony in this study. The DJI Matrice 600 Pro (M600) hexacopter was equipped with a pushbroom co-aligned VNIR-SWIR sensor (Headwall Photonics), which captures 640 spatial pixel scan lines with 546 spectral bands in the 400–2500 nm range. The M600 integrates three built-in navigation GPSs, alone with the APX-15 GNSS-inertial solution (Trimble Applanix) included in the hyperspectral system to provide positioning and orientation of the hyperspectral scanners, resulting in a final georeferencing accuracy of  $\pm 0.02$  m vertically and  $\pm 0.05$  m horizontally. However, this sensor has the disadvantage of providing VNIR and SWIR data as separate files, requiring stacking in a pre-processing step to integrate the complete VNIR-SWIR information.

The DJI Matrice 300 RTK (M300) quadcopter was equipped with a MicaSense RedEdge-MX dual multispectral sensor (MS), which captures spectral information with its 10 bands from the visible to near-infrared (NIR) regions (Román et al., 2022). This sensor incorporates a Down-welling Light Sensor (DLS2) to estimate changes in light conditions and solar angle during flight. In addition, the M300 was simultaneously equipped with the DJI Zenmuse L1 sensor, which integrates a LiDAR Livox module, a high-precision Inertial Measurement Unit (IMU), and a 20 MP optical RGB camera. This sensor was used to retrieve a high-resolution Digital Surface Model (DSM) for HS flight planning and pre-processing. For precise georeferencing accuracy, the M300 is equipped with on-board RTK technology.

Flight operations on Hannah Point were conducted on 18 February 2022, between 12:00 and 14:00 local time and under predominantly cloudy weather conditions. In order to perform post processing kinematic (PPK) georeferencing, a Reach RS2 + RTK GNSS antenna (EMLID) was used as a base station, providing horizontal and vertical measurements of 4 mm + 1 ppm and 8 mm + 1 ppm, respectively. Flight missions were planned using UgCS desktop software (SPH engineering, Latvia, v.4.14), with the LiDAR-based DSM used as a reference (GSD = 2.55 cm/px with an RMSE of 20 cm, 41 cm, 28 cm (x, y, z-axis, respectively)). The HS carried by the M600 provided an estimated ground sampling distance (GSD) of 7.5 cm/px, with a 40% lateral overlap. The MS carried by the

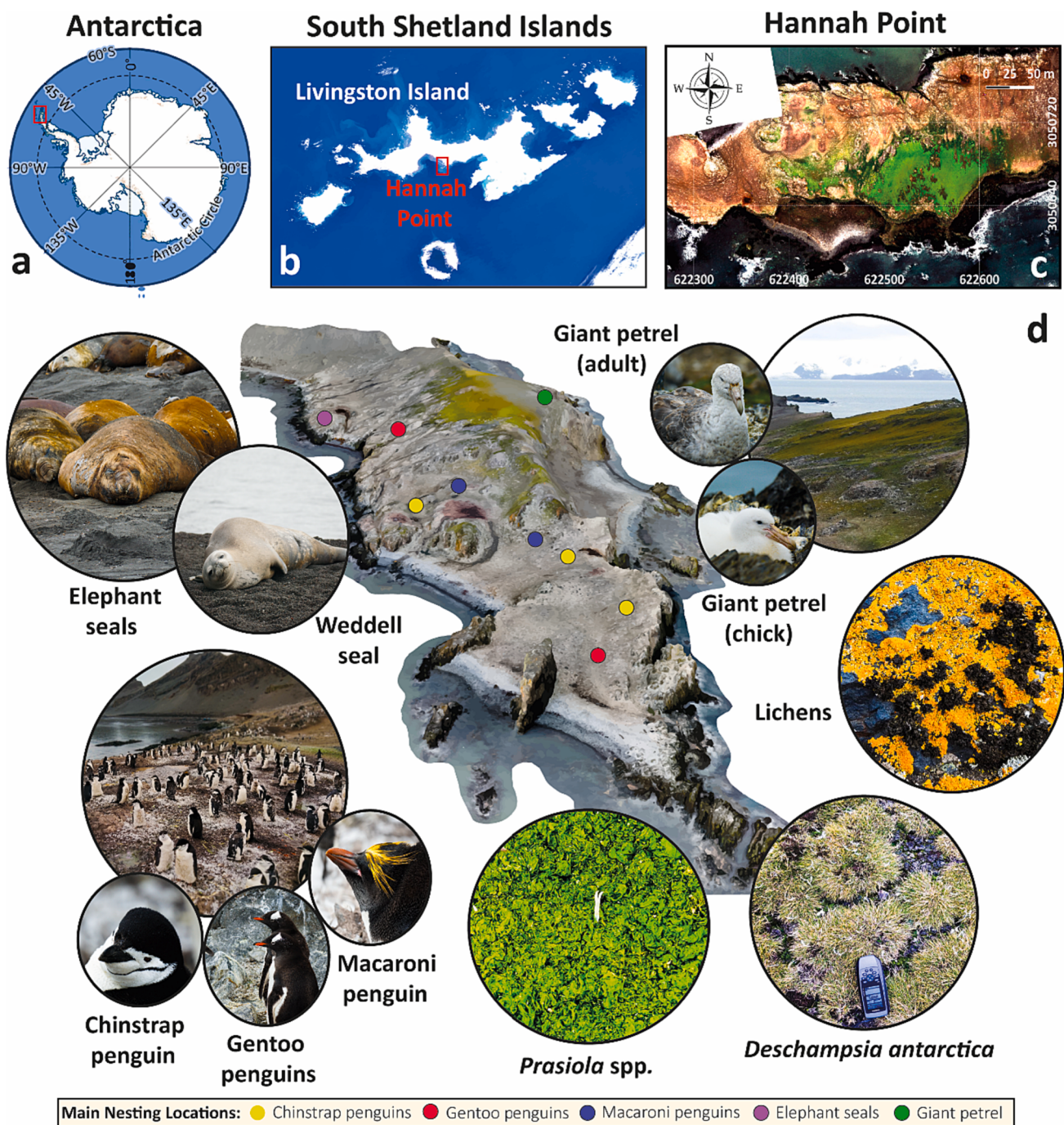


**Fig. 1.** (a) south shetland islands from the south pole. (b) Hannah Point penguin colony on Livingston Island. (c) RGB composite orthomosaic derived from UAV-based multispectral imagery over the Hannah Point penguin colony using bands red 668 nm, green 560 nm, and blue 475 nm. (d) Overview of the locations of some of the confirmed breeders and flora species at the Hannah Point penguin colony, using a 3D model derived from UAV imagery as a background map. The colored points represent the main nesting sites recognized by the [Antarctic Treaty Secretariat \(2023\)](#). (For interpretation of the references to color in this figure legend, the reader is referred to the web version of this article.)

M300 achieved an estimated GSD of 12.09 cm/px with 80% frontal and lateral overlap, respectively. Both sensors were radiometrically calibrated before the surveys, using a calibrated tarp ( $3 \times 3$  m) for the HS and a calibration panel for the MS.

Parallel to UAV flights, 35 ground spectra were measured using a USB2000 spectrometer (Ocean Insight, Florida, USA), which collected 1667 wavelength bands within the 320–876 nm range. The instrument was connected to a computer via a USB port, drawing its power directly from the host computer, and managed using the OceanView spectroscopy software (Ocean Insight, Florida, USA, v.20.0). Prior to the use of

the equipment, spectral calibration was performed in the laboratory under controlled environmental conditions, by varying light intensities for specific wavelengths. In the field, the measurement process began with a white reference, using a white fluopolymer known as “spectralon”, which possesses the highest diffuse reflectance of any known material. This reference was collected at every single field measurement to account for changes in ambient light intensity that could affect the readings. Subsequently, a black reference was collected at each sampling point by covering the instrument with a black container to correct for equipment-related noise in the measurements. Finally, measurements

were taken at each of the selected points of interest by holding the spectrometer at 1 m with respect the ground point with the aid of a 90° angle wooden stick, and setting manual integration times to control the range of reflectance values recorded. The calibration process was crucial in defining the peaks in the measurements, as in the ever-changing environmental conditions of the Antarctic continent, factors like temperature and cloud cover can affect the results obtained. These spectra served as a reference spectral library to identify the primary distinctive features of this penguin colony based on their spectral information. In fact, the species identified on the ground were analyzed and validated in the field.

### 2.3. Multispectral SfM photogrammetry

A Structure from Motion (SfM) photogrammetry process was implemented to produce final reflectance, which range from 0 to 1 (dimensionless), for the multispectral flight. The software used for this purpose was Agisoft Metashape v.1.8.4 (Agisoft LLC, St. Petersburg, Russia). Upon importing all UAV captures, a sparse point cloud was constructed through the “image alignment” step, employing the most accurate setting parameters available. Subsequently, a “3D dense cloud” was generated by using the aforementioned aligned captures. An interpolated Digital Surface Model (DSM) and a Digital Terrain Model (DTM) were then derived from the “3D dense cloud”. Finally, the orthomosaic was rendered using the DSM as a reference surface. The coordinate system used for all photogrammetric process-derived products was WGS84 / UTM zone 20S (EPSG: 32720).

### 2.4. Hyperspectral data processing

This section summarizes the entire processing workflow that was followed to handle HS products (Fig. 2). The SpectralView (Headwall Photonics, v.3.2.0) software was used for data preparation, which involved processing the VNIR and SWIR data cubes separately. Finally, the ENVI software (L3Harris Geospatial Solutions, Inc. Broomfield, CO, USA, v.5.3.6) was employed for data exploration and spectral analysis steps. To ensure consistency with the MS imagery, we used the same

projected coordinate system (WGS84 / UTM zone 20S, EPSG: 32720) for the HS data.

#### 2.4.1. Data preparation

The VNIR and SWIR data cubes were processed using SpectralView software, following a four-step processing workflow, which involved:

- (1) Conversion of raw data to radiance. The dark spectrum reference, which was collected on the ground by covering the sensor after the UAV survey, was subtracted from the digital numbers (DNs), and thus considered as sensor noise.
- (2) Conversion of radiance to reflectance. Using the radiometric-calibrated tarp reflectance measurement as a reference, this processing step built the empirical line calibration equation that best fits with the radiance captured by the sensor (Barreto et al., 2019; Wang & Myint, 2015). This technique assumed that the tarp reflectance measurement was uniform and did not change.
- (3) Hypercubes orthorectification. Orthorectification was performed to transform the central projection of each capture into an orthogonal ground view, without considering distorting effects related to tilt and terrain relief. This process results in hypercubes that have a uniform scale, enabling precise distance and direction measurements. This was performed by combining a precision DSM with the data processed from the APX-15 and the antenna. The POSPac UAV software (Trimble Applanix, v.8.9) used the information provided by the antenna as inputs to create a smoothed best-estimated trajectory (SBET), achieving a position accuracy of less than 2 cm. The DSM used for orthorectification was previously retrieved from LiDAR imagery.
- (4) Hypercubes mosaicking and stacking. A single orthorectified reflectance mosaic is generated for the VNIR and SWIR, respectively. Both separate files are stacked together to compile the entire spectral range of the sensor, after the removal of the water vapour absorbance wavelengths (1350–1460 nm, 1790–1960 nm, and 2350–2500 nm) since they influence the electromagnetic radiation reaching the Earth's surface (Rajakumari et al., 2022).

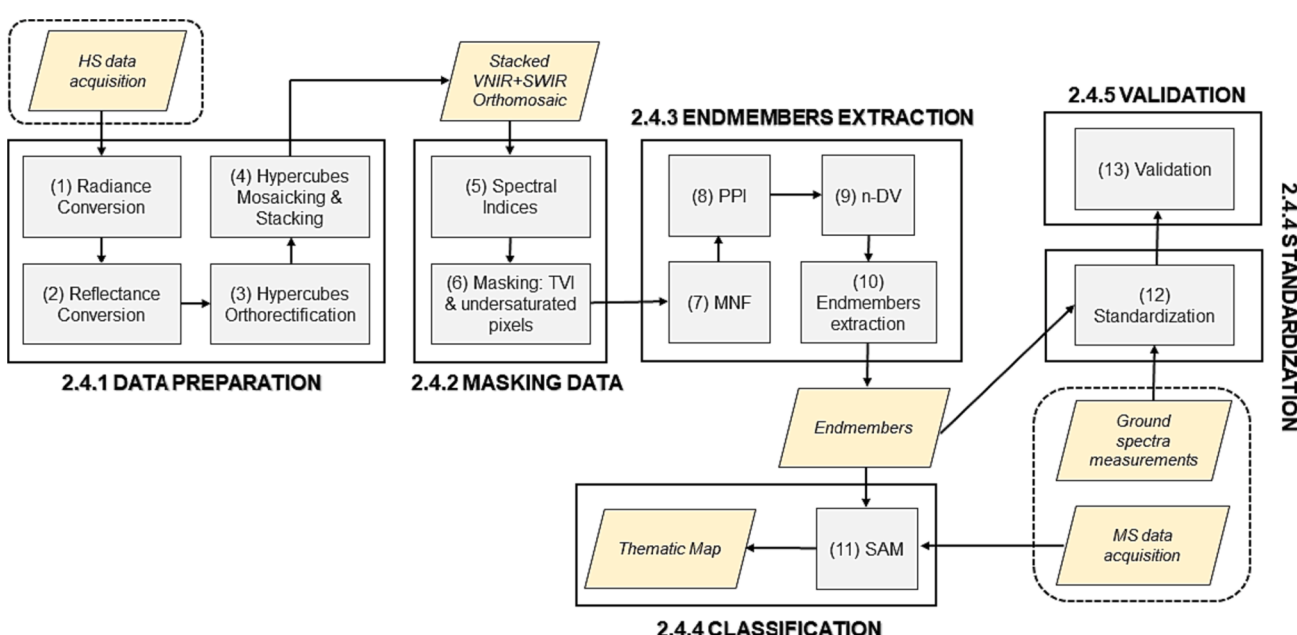


**Fig. 2.** Schematic representation of the hyperspectral processing steps followed in this study. Yellow boxes indicate data, while grey boxes indicate processes. Numbers represent the order of the processing workflow. HS: hyperspectral; MS: multispectral; TVI: triangular vegetation index; PPI: pixel purity index; MNF: minimum noise function; n-DV: n-dimensional visualizer; SAM: spectral angle mapper. (For interpretation of the references to color in this figure legend, the reader is referred to the web version of this article.)

#### 2.4.2. Masking data and spectral indices

Due to the large size of the dataset, a small region of interest was selected within the Hannah Point penguin colony, which included different visually identifiable terrain features, such as various vegetation communities, bare soil, guano, and rocks. To facilitate the endmember extraction and the subsequent classification, vegetation was separated from bare soil by using a mask based on various spectral indices. Among the available indices within the ENVI software, the Normalized Difference Vegetation Index (NDVI) (Rouse et al. 1973) and the Triangular Vegetation Index (TVI) (Broge & Leblanc, 2000) were selected due to their better performance in distinguishing vegetation coverage from terrain features in the region of interest. NDVI, which serves as a greenness indicator (Jimenez et al., 2022), relies on NIR and red wavelengths, centered at 860 nm and 649 nm, respectively. Through a band ratio approach, NDVI aims to standardize the influence of varying lighting conditions, surface slope, aspect, and other variables (Fretwell et al., 2011). TVI also functions as a narrowband indicator of vegetation greenness, that quantifies the radiant energy absorbed by leaf pigments by measuring the relative difference between red reflectance centered at 670 nm and red edge reflectance centered at 750 nm, along with the magnitude of reflectance in the green spectral range. TVI is computed as the area defined by the green peak, the near-infrared shoulder, and the lowest reflectance in the red region (Haboudane et al., 2004). The value of NDVI ranges from -1 to 1, with a common range for vegetation between 0.2 and 0.8. The TVI takes values between 0 and 30, using as threshold for vegetation those values above 3. In addition, a second mask was generated from the original hypercube to mask the under-saturated pixels.

#### 2.4.3. Endmember extraction

To extract the pure spectral signature of each class (endmember) needs to be extracted and used as input spectra for the classification of HS data. To achieve this, the Minimum Noise Fraction (MNF), the Pixel Purity Index (PPI), and the endmember extraction techniques were carried out. The MNF reduce the dataset's dimensionality by combining information from all bands in such a way that the output principal components are uncorrelated (Green et al., 1988; Luo et al., 2016). Consequently, only the first nine MNF bands were considered for the successive processing, discarding the bands containing just noise. The PPI technique finds the most spectrally pure pixels by repeatedly using n-dimensional scatterplots onto a 2D subspace to identify the least mixed spectral signatures (Chang et al., 2006). The PPI output is thresholded using the region of interest (ROI) tool, taking only the purest pixels into account as inputs for the n-Dimensional Visualizer (n-DV) scatter plot. The n-DV is an ENVI tool used to identify and cluster the purest pixels distributed in the n-D space and finally segregate them into their respective endmembers.

#### 2.4.4. Classification and spectral analysis

The supervised classification method Spectral Angle Mapper (SAM) was employed to identify pixels in the image spectra that match the retrieved endmembers during the hyperspectral data processing step. This algorithm calculates the angle between unknown and reference spectra to detect analogous spectral behaviour based on an angle threshold, in a space with dimensionality equal to the number of bands (Kruse et al. 1993). According to Kruse et al. (1993), it can be expressed using the following equation:

$$\alpha = \cos^{-1} \left[ \frac{\sum_{i=1}^{nb} t_i r_i}{\left( \sum_{i=1}^{nb} t_i^2 \right)^{\frac{1}{2}} \left( \sum_{i=1}^{nb} r_i^2 \right)^{\frac{1}{2}}} \right] \quad (1)$$

where  $t$  represents the spectrum for a pixel,  $r$  is the reference spectrum for a pixel,  $\alpha$  is the spectral angle between  $t$  and  $r$  (measured in radians or degrees), and  $n$  is the number of bands (Rossiter et al., 2020). In this study, SAM classifications of both HS and MS datasets were performed

using the ENVI software, by setting the previously mentioned angle threshold to 0.15 rad to reduce the variability between spectrally mixed endmembers. In the case of HS imagery, unidentified extracted endmembers were used as reference spectra. Conversely, supervised classification with the MS imagery was carried out using identified endmembers representing different vegetation communities and various ground features, after resampling the spectral libraries to match the wavelengths of the multispectral sensor.

Differences in absorption and reflection spectra between endmembers can be negligible, making the classification process difficult. Consequently, a spectral standardization method was applied to test the influence of the spectral shape on the classification process. The Band-max-min normalization method (Eq. (2)) suggested by Cao et al. (2017) was tested to minimize the variability in the reflectance amplitude, giving more value to spectral shape as a classification driver. This method was applied to compare and validate with ground spectra.

$$R_S(\lambda) = \frac{R_o - R_{(bandmin)}}{R_{(bandmax)} - R_{(bandmin)}} \quad (2)$$

$R_S$  is the standardized spectra,  $R_o$  is the original reflectance value,  $R_{bandmax}$  is the band corresponding to the maximum reflectance value, and  $R_{bandmin}$  is the band corresponding to the minimum reflectance value.

#### 2.4.5. Validation

An accuracy assessment was performed to validate the thematic maps generated using a stratified random sampling design, following Oloffson et al. (2014). As a result, an error matrix and statistical parameters such as the Cohen's Kappa coefficient, the User Accuracy (U-Acc), the Producer Accuracy (P-Acc), and the Overall Accuracy (OA) were calculated (Congalton & Green, 2009). This approach involves assessing the classification raster by comparing it with "real" maps using a stratified random sampling method. The OA is calculated by dividing the sum of the values along the main diagonal of the error matrix by the total number of sampled units. An OA value exceeding 80% is indicative of good and reliable results. The Cohen's Kappa Index, on the other hand, measures the difference between the observed agreement in the error matrix and the chance agreement, which is based on the row and column totals. This index can assume values ranging from -1 to +1, with results closer to +1 indicating better performance. User accuracy assesses the model's capacity to minimize false negatives, whereas producer accuracy evaluates the model's capability to minimize false positives.

All endmember spectra were compared to the ground spectra by considering only the available wavelengths between 400 and 876 nm to identify features based on their spectral characteristics. The Spectral Analyst tool from ENVI was used to calculate the similarity of each endmember with all the ground spectra. This tool combines the Spectral Angle Mapper and Spectral Feature Fitting (SFF) algorithms to rank the similarity of an unknown spectrum to a reference spectral library, providing a ranked score indicating the closest spectral similarity. To improve the precision of the analysis, it was focused on the wavelength range containing the main absorption features of the endmembers. In addition, the standardized endmember spectra were assessed as function of standardized ground spectra using linear regression within the programming language Python (Van Rossum & Drake, 1995). To assess the level of correlation, various statistical methods were employed, including the Root Mean Square Error (RMSE, Seegers et al., 2018, Eq. 3), the Pearson's correlation test and the Student's *t*-test. The Pearson's correlation test measures the linear relationship between two variables, with values close to -1 or +1 indicating a strong linear association between the two variables (Kirch, 2008, Eq. (4)). The Student's *t*-test, on the other hand, compares the means between two variables, determining whether the difference between them is statistically significant. If a significance level of *p*-values < 0.05 is assumed, then the result can be

considered statistically significant (Mishra et al., 2019).

$$RMSE = \sqrt{\frac{\sum_{i=1}^n (O_i - M_i)^2}{n}} \quad (3)$$

$$Pearsonr = \frac{n(\sum O_i M_i) - (\sum O_i)(\sum M_i)}{\sqrt{[n \sum M_i^2 - (\sum M_i)^2][n \sum O_i^2 - (\sum O_i)^2]}} \quad (4)$$

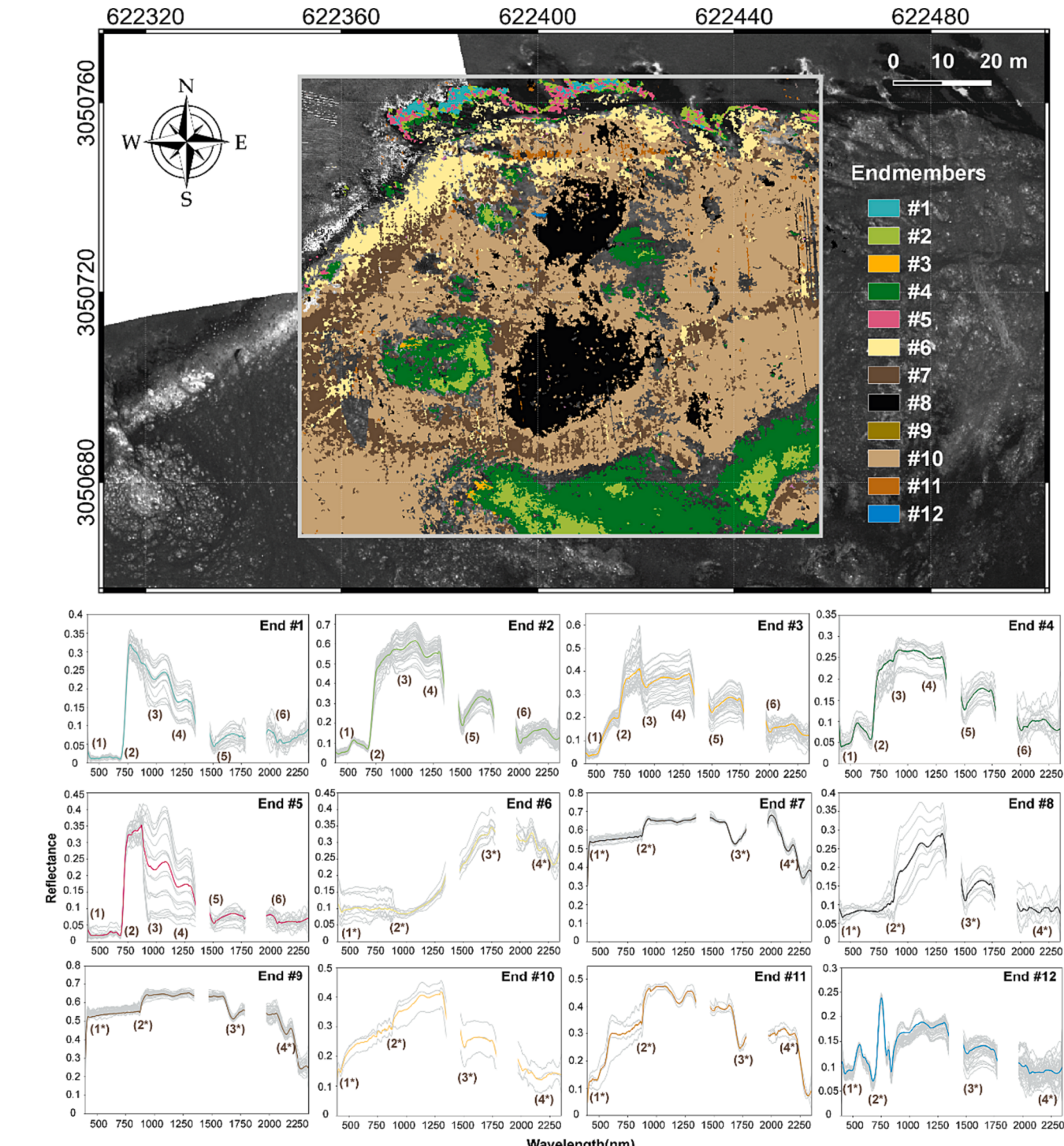


**Fig. 3.** SAM thematic map generated with the HS data. The spectral profiles for vegetation (endmembers 1–5) and ground (endmembers 6–12) features are also displayed along with solid lines indicating the average spectra, respectively. The water vapour absorbance regions (1350–1460 nm and 1790–1960 nm) were excluded from the HS processing. The numbers in brackets indicate absorption peaks (minimum reflectance values).

### 3. Results

#### 3.1. Endmembers extraction and classification

Twelve endmembers were retrieved as a result of the HS processing, using the VNIR bands to detect the vegetation taxa (five endmembers), while the SWIR bands were employed to detect the ground features (seven endmembers). In fact, SWIR bands have been widely documented for mapping mineral absorption features (Black et al., 2016; Keresztri et al., 2018), as well as regulating differences among guano spectra (Rees et al., 2017). The resulting SAM thematic map from the classification process is displayed in Fig. 3, along with the entire spectral signatures of the detected endmembers. The overall accuracy of the classification was 92.37 %, while the Cohen's Kappa coefficient was 0.73 (Supplementary Materials Table A).

The five endmembers associated with vegetation features (end-members 1–5) show the typical spectral behaviour of photosynthetic organisms, with a strong absorption peak in the red region (peak 2 at 669 nm) and a significant increase in reflectance from the red-edge region (700–750 nm), maintaining high values in the entire SWIR region (1000–2350 nm). In addition, repeated absorption peaks between vegetation endmembers were highlighted in the SWIR region (peak 3 at 943 nm, peak 4 at  $1190 \pm 20$  nm, peak 5 at 1523 nm, and peak 6 at 2025 nm).

On the contrary, the ground at Hannah Point is characterized by a moist mixture of guano, fish-based and krill-based vomit, mud and stagnant water in small pools. For this reason, it is challenging to quantify spectral differences between the seven ground endmembers (endmembers 6 to 12), with variable absorption peaks between them presenting important quantitative differences ( $\pm 10$  nm) in the SWIR region (peak 1\* at 480 nm, peak 2\* at 740 nm, peak 3\* at 1680 nm, and peak 4\* at 2100 nm).

#### 3.2. Endmembers identification and validation

The Spectral Analyst tool and the field identifications (Supplementary Materials Fig. B) were used to match the corresponding endmembers spectra with the collected spectral library from spectrometry (VNIR region between 400 and 876 nm). Although a good correspondence was not obtained in the Spectral Analyst for endmember 5, the SAM classification revealed its location on the coastline. Therefore, based on field identification, it is believed that this endmember corresponds to the species of red macroalgae *Pyropia* *endiviifolia*. Much better correspondence was obtained for the rest of the vegetation endmembers using the Spectral Analyst. For example, the crustose lichen *Caloplaca* s. lat., which was evidently identifiable as endmember 3, was also validated with field identification (Supplementary Materials Fig. B, PH24 and PH25). Regarding the vascular plants and the terrestrial alga *Prasiola* spp., the Spectral Analyst hindered their identification between end-members 2 and 4, due to a greater spectral homogeneity. The spectral similarity between the vascular plant species *Deschampsia antarctica* and *Collobanthus quitensis*, as described in Chi et al. (2021), is also evident in this study, and they have been considered together as tracheophytes. By using both field identification (Supplementary Materials Fig. B, PH29 for *Collobanthus quitensis*, PH30 for *Deschampsia antarctica*, and PH14 for *Prasiola* spp.) and the endmembers' location based on the SAM classification, it was possible to associate endmember 2 with tracheophytes and endmember 4 with *Prasiola* spp.

Regarding the ground endmembers, the Spectral Analyst at both analyzed regions of the electromagnetic spectrum and the field identification (Supplementary Materials Fig. B, PH1, PH2 and PH3) clearly associate endmember 12 with a small water lagoon covered by green algae inside a chinstrap penguin guano stain. Although the Spectral Analyst results inconclusive for endmembers 6–12, field identification allows the assumption that endmember 6 corresponds to beach sand, endmembers 7, 9, 10, and 11 with different bare soil classes

(Supplementary Materials Fig. B, PH31, PH32 and PH33), and end-member 8 with the muddy guano (Supplementary Materials Fig. B, PH7 and PH10).

Accuracy metrics indicated that there was a satisfactory consistency between the HS identified endmembers and the field spectrometry (Fig. 4). The low RMSE values suggested that there were small differences between the compared spectra for all identified taxa, particularly with *Prasiola* spp., and *Caloplaca* s. lat. This was further supported by the Pearson's correlation test, which showed values close to unity in most cases, indicating an almost perfect positive correlation for all analyzed vegetation classes. The p-values for all classes were also below the 0.05 significance level, indicating that there was a statistically significant similarity between the compared spectra.

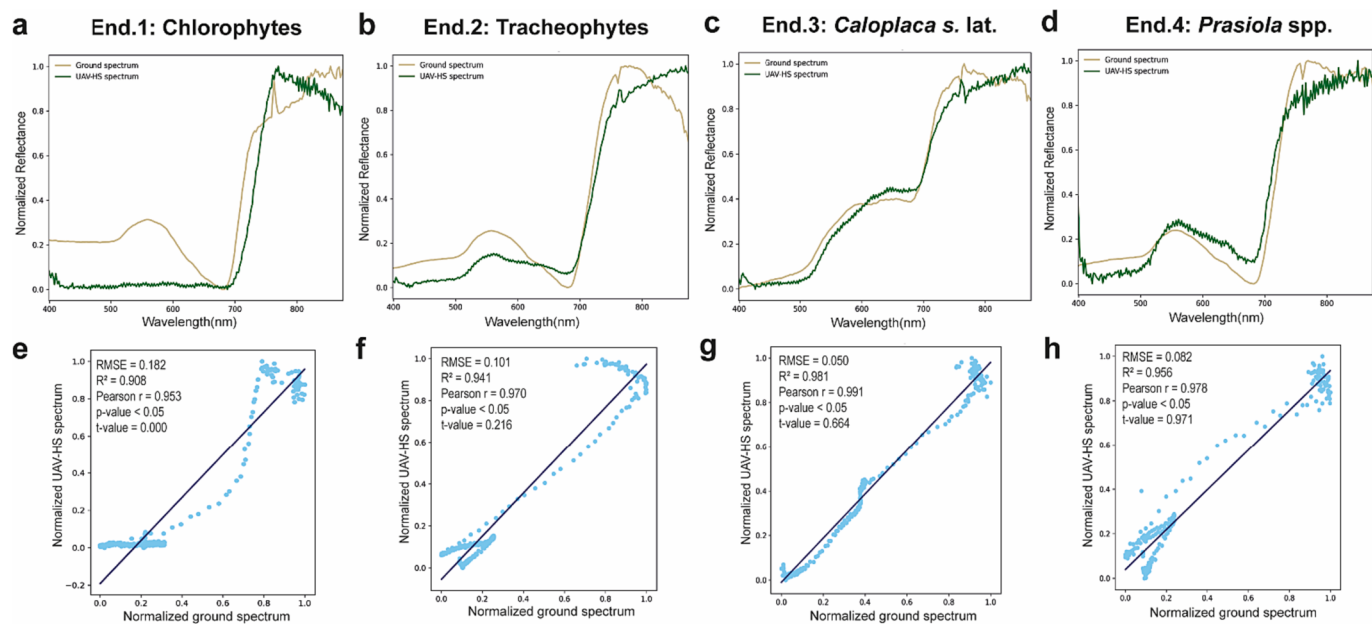
#### 3.3. Hannah Point's vegetation communities spectral library

Fig. 5 illustrates the resulting spectral library for the main identified vegetation communities at Hannah Point penguin colony in the 400–2500 nm wavelength range derived from around 245 pure pixels spectra retrieved with HS imagery.

In general, the spectral behaviour of vegetation communities shows two small absorption features in the NIR region, less pronounced than the absorption peaks found in the SWIR region. As shown in Fig. 5, green vegetation presents a chlorophyll maximum absorption peak at 669 nm, and is highly reflective in the green wavelength ranges. The orange lichen *Caloplaca* s. lat. shows low reflectance values in the lower region of the spectrum, but a higher reflective absorption peak at 669 nm compared to green vegetation. On the other hand, the red alga *Pyropia* *endiviifolia* shows low reflectance values in the blue-green region of the spectrum, acquiring the characteristic dark red color. The small water pool has been included in this vegetation analysis due to the presence of a complex mixture of photosynthetic microorganisms that shows some of the main vegetation spectral features such as the absorption peak at 669 nm or the two strong absorption peaks in the SWIR region (1520 nm and 2050 nm, approximately), despite the influence of water that generated a strong decay in the NIR region of the spectrum.

#### 3.4. Resampling hyperspectral data for multispectral analysis

The spectral library obtained from the HS imagery was adjusted to the MS sensor wavelengths through spectral resampling to enable its application in characterizing the entire Hannah Point penguin colony. Fig. 6 shows the SAM thematic map that resulted from the use of the HS-identified endmembers on the MS data, which obtained an Overall Accuracy of 89.54% and a Cohen's Kappa coefficient of 0.66 (see Supplementary Materials Table B). Although all vegetation classes were classified correctly, frequent missclassifications occurred between *Prasiola* spp., tracheophytes, and chlorophytes, especially in wet intertidal areas where their spectral behaviour is affected by humidity and seawater. Tracheophytes predominate on an area of 0.54 ha, particularly on the steep slope that characterizes the topography of Hannah Point, while *Prasiola* spp. predominates on an area of 0.58 ha, as it is more abundant relatively close to the guano stains. On the other hand, the small patches of *Caloplaca* s. lat. detectable through the UAV-equipped sensor cover an area of 25 m<sup>2</sup>, although it would not be indicative of the total coverage of this lichen as it also extends on the vertical rocks surface. Some visual patterns in the ground composition appeared well-defined, particularly in the main nesting areas. Three different bare soil classes were identified with the supervised classification, probably corresponding to the different nature of the substrate. However, the lack of ground reference spectra, alongside the joint effect of the intense fauna activity and the topographic characteristics of Hannah Point, can complicate not only the validation of these end-members but also classification accuracy. In addition, the moist mixture of mud, penguin waste, and soil makes it difficult to assign one specific class to "muddy guano" as with hyperspectral imagery.



**Fig. 4.** Validation of the identified endmembers using field spectrometry across the 400 nm to 875 nm wavelength range. A scatter plot with regression lines (a–d) and the resulting accuracy metrics from this statistical validation (e–h) are also displayed in the figure for each identified endmember, respectively.

#### 4. Discussion

The detection of guano acquires greater importance due to its ecological role in the entire Antarctic ecosystem. Unlike other Antarctic penguin colonies analyzed through remote sensing techniques, such as Vapour Col (Román et al., 2023) or Penguin Island (Zmarz et al., 2018), where guano stains appear well-defined as pink or orange spots on the substrate, surface runoff due to the characteristic slope of the terrain at Hannah Point and the movement of fauna from sea to land and vice-versa, causes the entire substrate to be constantly wet and mixed. Consequently, endmember 8 could be identified as chinstrap penguin guano, although it is heavily mixed with the soil. The only complete spectral library of guano (VNIR + SWIR) published to date for chinstrap penguins (Rees et al., 2017) was compared to endmember 8, revealing some similar spectral features but with significant differences (Supplementary Materials Fig. C). Lower reflectance values for endmember 8 are clearly associated to wetter conditions at Hannah Point penguin colony. However, the main absorption features that determines the differences between guano spectra in both cases are the same, particularly peak 2 at 1200 nm and peak 3 at 1450 nm. Nonetheless, the absorption feature at 550 nm, which is responsible for the pink coloration of chinstrap penguin guano due to a diet primarily consisting of krill (Rees et al., 2017), is not observable in the spectral signature of endmember 8. This is due to the mixing of other soil components that exhibit lower reflectance values in this region of the spectrum.

Recent evidence has shown the existence of nutrient hotspots near penguin colonies that promote plant growth (Bokhorst et al., 2021), and determine the spatial zonation of vegetation in the terrestrial region of Maritime Antarctica. Given the impacts of global climate change, penguin breeding site movements can result in high colony losses, which directly and indirectly affect vegetation communities. Therefore, monitoring these communities is essential for understanding trends and future environmental implications. The high nitrogen content, while potentially toxic for some species, enables the establishment of particular bryophytes, lichens, and algae. In that sense, and regarding antarctic ecosystems, species within the genus *Caloplaca*, *Xanthoria*, and *Mastodia* among other lichens, and within the genus *Prasiola* among terrestrial algae, typically dominate nitrogen-enriched areas (ornithogenic vegetation). This study provides valuable data in terms of both

spectral information and spatial distribution of some of the most prominent terrestrial and intertidal photosynthetic organisms inhabiting the proximities of a penguin colony. It also proves the characteristic zonation described by Smykla et al. (2007), with small mats of *Prasiola* spp. in the nutrient-rich areas near the main nesting points. Similarly, the orange lichen *Caloplaca* s. lat. and the chlorophyte algae frequently appear as small patches on vertical rocks distant from the nesting areas, likely fertilized by seabirds perching on them. On the other hand, tracheophytes are located in the steeper areas, that are not so heavily disturbed by fauna activity, with *Deschampsia antarctica* being the most dominant species with small mats of *Collobanthus quitensis*.

The information about the composition of the vegetation cover was derived from their spectral behaviour. Green vegetation, with chlorophyll-a and b as main photosynthetic pigments, and without other pigment-dominated surface layer, can be easily recognized by the valley around 680 nm caused by strong chlorophyll absorption in that region, and by an increase in reflectance in the NIR around 800 nm, where they no longer absorb. However, the rest of vegetation communities have been clearly distinguished, as the main absorption/reflection features in the visible range are associated with pigment composition. The red macroalgae *Pyropia endiviifolia* also contains chlorophyll a, but not chlorophyll b, and relatively high values of some carotenoids such as lutein (García-Plazaola et al., 2022a). It has a maximum absorption band in the range of 400–600 nm mainly due to the red phycoerythrins. In addition, the absence of chlorophyll b and the presence of phycoerythrins typical of rhodophytes, gives them their characteristic dark reddish appearance, with low reflectance values in the blue-green region of the spectrum (Douay et al., 2022). The orange lichen *Caloplaca* s. lat. was easily distinguishable due to its high content of parietin on the thallus surface (Solhaug & Gauslaa, 1996), an orange pigment with a maximum absorption peak at around 480 nm, resulting in low spectral reflectance in the blue region of the spectrum and high reflectance in the orange and red regions, which partially masks the characteristic absorption valley at 680 nm. This is more evident in wet thalli, as already observed for other Antarctic species of the same group containing parietin, such as *Xanthoria elegans* (Miloš et al., 2018). The greatest difficulties arise when trying to differentiate amongst tracheophytes, chlorophytes and *Prasiola* spp., as their chlorophylls and carotenoids composition and proportion is very similar (García-Plazaola et al.,

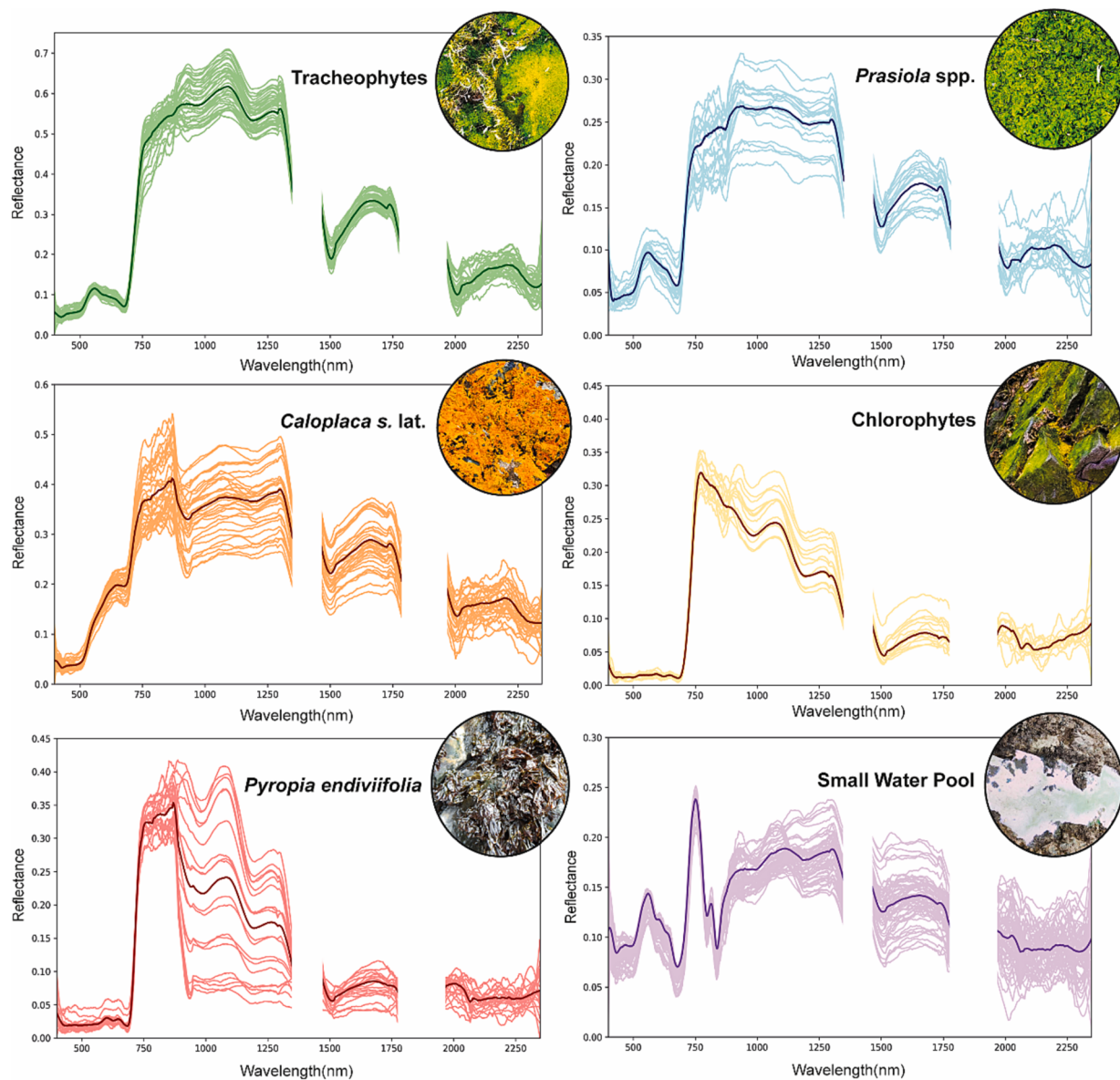


**Fig. 5.** Hannah Point vegetation spectral library. The spectral signatures of all pure pixels for each vegetation species are represented, with the average spectra highlighted. The water vapour absorbance regions (1350–1460 nm and 1790–1960 nm) were excluded from the HS processing.

2022b; Fernández-Marín et al., 2019; Sáez et al., 2019). Chlorophyll-a and b as predominant pigments leads to absorption peaks at the blue (400–500 nm) and red (600–650 nm), resulting in low reflectance values in those regions of the spectrum. However, generally higher reflectance values and two absorption peaks at 1000 nm and 1250 nm, related to water content and the physical structure of the tissues, allow Tracheophytes to be separated from *Prasiola* spp.

This study represents the first attempt to use UAV-based HS data to identify the main vegetation and ground features of Antarctic penguin colonies. It was also degraded to MS data to facilitate feature identification at a larger coverage. However, the poorer spectral resolution of MS data led to more missclassification errors, particularly when it came to green-leaved vegetation. In fact, some absorption features of vegetation communities rely on specific spectral wavelengths only accessible by HS sensors, resulting in higher classification accuracies than the MS sensors. However, to determine vegetation community coverage and track them, the VNIR region is enough to identify them by their spectral reflectance, making the MS sensor the most appropriate. On the other hand, for geological studies where the intrinsic signal of SWIR has

greater potential for soil/rock type identification and characterization, the HS is thus essential. We have identified UAV remote sensing as a powerful tool for accurately monitoring changes in environmental communities, and we provide advice for the next generation of UAV-based hyperspectral and multispectral sensors.

## 5. Conclusions

We have demonstrated the potential of UAV-based HS technology to identify and map the main terrestrial features of an Antarctic penguin colony through the detection of small spectral differences in their reflectance signatures. Around 245 pure pixels spectra across the Hannah Point penguin colony were collected to generate a precise spectral library of the vegetation communities in the full spectral range between 400 and 2500 nm. Consequently, we identified two wavelength regions, namely in the green (495–570 nm) and NIR (800–900 nm), for their valuable contribution to vegetation discrimination based on pigments composition. In addition, the moist mixture composed of penguin waste, mud, and stagnant water, known as “muddy guano” in this study, was

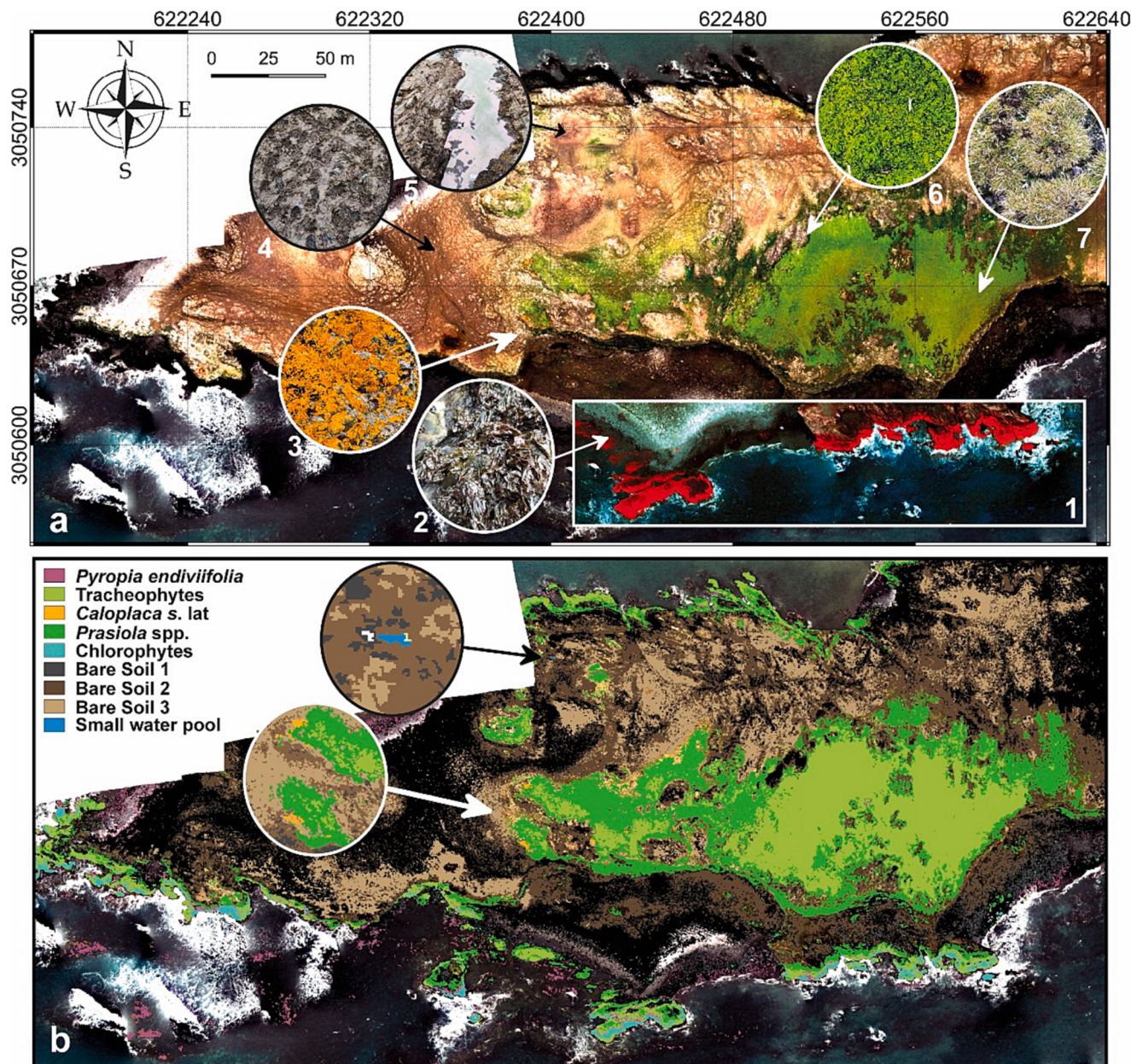


**Fig. 6.** (a) RGB composite (red 650 nm, green 560 nm, and blue 475 nm) of the Hannah Point MS orthomosaic. In addition, detailed captures are indicated by numbers: (1) false colour composite (NIR 840 nm, red 650 nm, and green 560 nm) in the coastal fringe revealing vegetation communities in red colour; (2) the red macroalga *Pyropia endiviifolia*; (3) the crustose lichen *Caloplaca s. lat.*; (4) muddy guano; (5) a water lagoon in the penguin nesting area; (6) the terrestrial alga *Prasiola spp.*; and (7) the tracheophyte species *Deschampsia antarctica*. (b) SAM thematic map generated by applying the HS-identified endmembers to the MS data. (For interpretation of the references to color in this figure legend, the reader is referred to the web version of this article.)

also spectrally characterized and analyzed through comparison with existing literature, revealing the appearance of the most commonly used absorption feature at 1450 nm to differentiate penguin species based on guano composition. One of the main goals of this study was the capacity to downscale the spectral library to MS imagery by applying a supervised classification method with a high level of accuracy, providing new proxies for vegetation communities that could avoid the ongoing efforts to repeat all the HS processing steps in different penguin colonies across Antarctica. We also proved the existence of an ecological gradient structure in the zonation of vegetation communities chiefly dependent on nutrient-rich guano inputs at penguin colonies, with a predominant coverage of *Prasiola spp.* distributed in small patches around the main nesting points.

#### Declaration of Competing Interest

The authors declare that they have no known competing financial interests or personal relationships that could have appeared to influence the work reported in this paper.

#### Data availability

No data was used for the research described in the article.

#### Acknowledgements

The authors thank the crew of the BIO Hespérides oceanographic vessel and the Marine Technology Unit (UTM-CSIC) for their logistic

support. We also thank D. Roque for supporting UAV operations. This research was funded by the Spanish Government projects RTI2018-098048B-100 and PID2021-1257830B-100. Equipment was funded by Spanish Government Infraestructure projects EQC2018-004446-P, EQC2018-004275-P and EQC2019-005721. A. Román is supported by grant FPU19/04557 funded by Ministry of Universities of the Spanish Government. B. Fernández-Marín is supported by RYC2021-031321-I grant funded by MCIN/AEI/10.13039/501100011033 and by the European Union NextGenerationEU/PRTR. This work represents a contribution to CSIC Thematic Interdisciplinary Platforms POLARCSIC and PTI TELEDETECT.

## Appendix A. Supplementary material

Supplementary data to this article can be found online at <https://doi.org/10.1016/j.jag.2023.103565>.

## References

- Ancel, A.R., Cristofari, R., Trathan, P.N., Gilbert, C., Fretwell, P.T., Beaulieu, M., 2017. Looking for new emperor penguin colonies? Filling the gaps. *Glob. Ecol. Conserv.* 9, 171–179. <https://doi.org/10.1016/j.gecco.2017.01.003>.
- Antarctic Treaty Secretariat, 2023. Hannah Point. Antarctic Treaty Visitor site guidelines website. In: <https://www.ats.aq/devAS/Ats/VisitorSiteGuidelines?lang=e> (Last Accessed 09/03/2023).
- Atala, C., Pertierri, L.R., Aragón, P., Carrasco-Urra, F., Lavín, P., Gallardo-Cerdá, J., Ricote-Martínez, N., Torres-Díaz, C., Molina-Montenegro, M.A., 2019. Positive interactions among native and invasive vascular plants in Antarctica: assessing the “nurse effect” at different spatial scales. *Biol. Invas.* 21, 2819–2836. <https://doi.org/10.1007/s10530-019-02016-7>.
- Atkinson, A., Hill, S.L., Pakhomov, E.A., Siegel, V., Reiss, C.S., Loeb, V.J., Steinberg, D.K., Schmidt, K., Tarling, G.A., Gerrish, L., Sailley, S.F., 2019. Krill (*Euphausia Superba*) distribution contracts southward during rapid regional warming. *Nat. Clim. Change.* 9, 142–147. <https://doi.org/10.1038/s41558-018-0370-z>.
- Barber-Meyer, S.M., Shannon, M., Kooyman, G.L., Ponganis, P.J., 2007. Estimating the relative abundance of emperor penguins at inaccessible colonies using satellite imagery. *Polar Biol.* 30, 1565–1570. <https://doi.org/10.1007/s00300-007-0317-8>.
- Barbosa, A., De Mas, E., Benzal, J., Diaz, J.I., Motas, M., Jerez, S., Pertierri, L., Benayas, J., Justel, A., Lauzurica, P., García-Peña, F.J., Serrano, T., 2013. Pollution and Physiological variability in gentoo penguins at two rookeries with different levels of human visitation. *Antarct. Sci.* 25 (2), 329–338. <https://doi.org/10.1017/S0954102012000739>.
- Barreto, M.A.P., Johansen, K., Angel, Y., McCabe, M.F., 2019. Radiometric assessment of a UAV-based push-broom hyperspectral camera. *Sensors.* 19, 4699. <https://doi.org/10.3390/s19214699>.
- Belyaev, O., Sparaventi, E., Navarro, G., Rodríguez-Romero, A., Tovar-Sánchez, A., 2023. The contribution of penguin guano to the Southern Ocean iron pool. *Nat. Com.* 14, 1781. <https://doi.org/10.1038/s41467-023-37132-5>.
- Bird, C.N., Dawn, A.H., Dale, J., Johnston, D.W., 2020. A semi-automated method for estimating Adélie penguin colony abundance from a fusion of multispectral and thermal imagery collected with unoccupied aircraft systems. *Remote Sens.* 12, 3692. <https://doi.org/10.3390/rs12223692>.
- Black, C.E., 2016. A comprehensive review of the phenology of *Pygoscelis* penguins. *Polar Biol.* 39, 405–432. <https://doi.org/10.1007/s00300-015-1807-8>.
- Black, M., Riley, T.R., Ferrier, G., Fleming, A.H., Fretwell, P.T., 2016. Automated lithological mapping using airborne hyperspectral thermal infrared data: a case study from Anchorage Island, Antarctica. *Remote Sens. Environ.* 176, 225–241. <https://doi.org/10.1016/j.rse.2016.01.022>.
- Bokhorst, S., Convey, P., van Logtestijn, R., Aerts, R., 2021. Temperature impact on the influence of penguin-derived nutrient and mosses on non-native Grass in a simulated polar ecosystem. *Glob Chang Biol.* 28, 816–828. <https://doi.org/10.1111/gcb.15979>.
- Broge, N.H., Leblanc, E., 2000. Comparing prediction power and stability of broadband and hyperspectral vegetation indices for estimation of green leaf area index and canopy chlorophyll density. *Remote Sens. Environ.* 76, 156–172. [https://doi.org/10.1016/S0034-4257\(00\)00197-8](https://doi.org/10.1016/S0034-4257(00)00197-8).
- Brown, J.A., 2018. Remote Sensing of Penguin Populations: Development and Application of a satellite-based Method. University of Cambridge. Doctoral Thesis in Philosophy.
- Cao, F., Yang, Z., Ren, J., Jiang, M., Ling, W.K., 2017. Does normalization methods play a role for hyperspectral image classification? arXiv preprint arXiv: 1710.02939. DOI: 10.48550/arXiv.1710.02939.
- Cao, J., Liu, K., Zhuo, L., Liu, L., Zhu, Y., Peng, L., 2021. Combining UAV-based hyperspectral and LiDAR data for mangrove species classification using the rotation forest algorithm. *Int. J. Appl. Earth Obs. Geoinf.* 102, 102414 <https://doi.org/10.1016/j.jag.2021.102414>.
- Chi, J., Lee, H., Hong, S.G., Kim, H., 2021. Spectral characteristics of the Antarctic vegetation: a case study of Barton peninsula. *Remote Sens.* 13, 2470. <https://doi.org/10.3390/rs13132470>.
- Colesie, C., Walshaw, C.V., Garcia-Sancho, L., Davey, M.P., Gray, A., 2022. Antarctica's vegetation in a changing climate. *WIREs Clim. Change.* e810 <https://doi.org/10.1002/wcc.810>.
- Congalton, R., Green, K., 2009. Assessing the Accuracy of Remotely Sensed Data: Principles and Practices, second ed. CRC/Taylor & Francis, Boca Raton.
- Convey, P., 2011. Antarctic terrestrial biodiversity in a changing world. *Polar Biol.* 34, 1629–1641. <https://doi.org/10.1007/s00300-011-1068-0>.
- Convey, P., Chowin, S.L., Clarke, A., Barnes, D.K.A., Bokhorst, S., Cummings, V., Ducklow, H.W., Frati, F., Allan Green, T.G., Gordon, S., Griffiths, H.J., Howard-Williams, C., Huiskes, A.H.L., Laybourn-Parry, J., Berry Lyons, W., McMinn, A., Morley, S.A., Peck, L.S., Quesada, A., Robinson, S.A., Schiaparelli, S., Wall, D.H., 2014. The spatial structure of Antarctic biodiversity. *Ecol. Monogr.* 84 (2), 203–244. <https://doi.org/10.1890/12-2216.1>.
- Douay, F., Verpoorter, C., Duong, G., Spilmont, N., Gevaert, F., 2022. New hyperspectral procedure to discriminate intertidal macroalgae. *Remote Sens.* 14, 346. <https://doi.org/10.3390/rs14020346>.
- Dunn, M.J., Adlard, S., Taylor, A.P., Wood, A.G., Trathan, P.N., Ratcliffe, N., 2021. Uncrewed aerial vehicle population survey of three sympatrically breeding seabird species at Signy Island, South Orkney Islands. *Polar Biol.* 44, 717–727. <https://doi.org/10.1007/s003000021-02831-6>.
- Durán, J., Rodríguez, A., Heiðmarsson, S., Lehmann, J.R.K., Del Moral, A., Garrido-Benavent, I., De los Ríos, A., 2021. Cryptogamic cover determines soil attributes and functioning in polar terrestrial ecosystems. *Sci. Total Environ.* 762, 143169. doi: 10.1016/j.scitotenv.2020.143169.
- Fernández-Marín, B., López-Pozo, M., Perera-Castro, A.V., Arzac, M.I., Sáenz-Ceniceros, A., Colesie, C., De los Ríos, A., Sancho, L.G., Pintado, A., Laza, J.M., Pérez-Ortega, S., García-Plazaola, J.I., 2019. Symbiosis at its limits: ecophysiological consequences of lichenization in the genus *Prasiola* in Antarctica. *Ann. Bot.* 124, 1211–1226. doi: 10.1093/aob/mzc149.
- Firla, M., Mustafa, O., Pfeifer, C., Senf, M., Hese, S., 2019. Intraseasonal variability of guano stains in a remotely sensed penguin colony using UAV and satellite. *ISPRS Ann. Photogramm. Remote Sens. Spat. Inf. Sci.* IV-2/W5, 111–118. <https://doi.org/10.5194/isprs-annals-IV-2-W5-111-2019>.
- Fretwell, P.T., Trathan, P.N., 2009. Penguins from space: faecal stains reveal the location of emperor penguin colonies. *Glob. Ecol. Biogeogr.* 18, 543–552. <https://doi.org/10.1111/j.1466-8238.2009.00467.x>.
- Fretwell, P.T., Trathan, P.N., 2020. Discovery of new colonies by Sentinel2 reveals good and bad news for emperor penguins. *Remote. Sens. Ecol. Conserv.* 7 (2), 139–153. <https://doi.org/10.1007/rse2.176>.
- Fretwell, P.T., Convey, P., Fleming, A.H., Peat, H.J., Hughes, K.A., 2011. Detecting and mapping vegetation distribution on the Antarctic Peninsula from remote sensing data. *Polar Biol.* 34, 273–281. <https://doi.org/10.1007/s00300-010-0880-2>.
- Fretwell, P.T., Philips, R.A., Brooke, M., Fleming, A.H., McArthur, A., 2015. Using the unique spectral signature of guano to identify unknown seabird colonies. *Remote Sens. Environ.* 156, 448–456. <https://doi.org/10.1016/j.rse.2014.10.011>.
- García-Plazaola, J.I., Arzac, M.I., Brazares, L., Fernández, J., Laza, J.M., Vilas, J.L., López-Pozo, M., Perera-Castro, A.V., Fernández-Marín, B., 2022a. Freezing and desiccation tolerance in the Antarctic bangiophyte *Pyropia endiviifolia* (*Rhodophyta*): a chicken and egg problem? *Eur. J. Phycol.* <https://doi.org/10.1080/09670262.2022.2136405>.
- García-Plazaola, J.I., López-Pozo, M., Fernández-Marín, B., 2022b. Xanthophyll cycles in the juniper haircap moss (*Polytrichum juniperinum*) and Antarctic hair Grass (*Deschampsia antarctica*) on Livingston Island (South Shetland Islands, Maritime Antarctica). *Polar Biol.* 45, 1247–1256. <https://doi.org/10.1007/s00300-022-03068-7>.
- Garrido-Benavent, I., De los Ríos, A., Fernández-Mendoza, F., Pérez-Ortega, S., 2017a. No need for stepping stones: Direct, joint dispersal of the lichen-forming fungus *Mastodia tessellata* (Ascomycota) and its photobiont explains their bipolar distribution. *J. Biogeogr.* 45, 213–224. doi: 10.1111/jbi.13105.
- Garrido-Benavent, I., Pérez-Ortega, S., De los Ríos, A., 2017. From Alaska to Antarctica: Species boundaries and genetic diversity of *Prasiola* (*Trebouxiophyceae*), a foliose chlorophyte associated with the bipolar lichen-forming fungus *Mastodia tessellata*. *Mol. Phylogenet. Evol.* 107, 117–131. <https://doi.org/10.1016/j.ymp.2016.10.013>.
- Green, A.A., Berman, M., Switzer, P., Craig, M.D., 1988. A Transformation for ordering multispectral data in terms of image quality with implications for noise removal. *IEEE Trans. Geosci. Remote Sens.* 26 (1), 65–74.
- Green, T.G.A., Schroeter, B., Sancho, L.G., 2007. Plant life in antarctica. In: Pugnaire, F. I., Valladares, F. (Eds.), Functional Plant Ecology, pp. 389–434. doi: 10.1201/9781420007626.CH13.
- Haboudane, D., Miller, J.R., Pattey, E., Zarco-Tejada, P.J., Strachan, I.B., 2004. Hyperspectral vegetation indices and novel algorithms for predicting green LAI of crop canopies: modeling and validation in the context of precision agriculture. *Remote Sens. Environ.* 90 (3), 337–352. <https://doi.org/10.1016/j.rse.2003.12.013>.
- Huang, J., Sun, L., Huang, W., Wang, X., Wang, Y., 2010. The ecosystem evolution of penguin colonies in the past 8500 years on Vostok Hills, East Antarctica. *Polar Biol.* 33, 1399–1406. <https://doi.org/10.1007/s00300-010-0832-x>.
- IAATO, 2015. Tourism Statistics. International Association of Antarctica Tour Operators (IAATO) website. In: <https://iaato.org/information-resources/data-statistics/visitor-statistics/visitor-statistics-downloads/> (Last Accessed 09/03/2023).
- Jimenez, R.B., Lane, K.J., Hutyra, L.R., Fabian, M.P., 2022. Spatial resolution of Normalized Difference Vegetation Index and greenness exposure misclassification in an urban cohort. *J. Expo. Sci. Environ. Epidemiol.* 32, 213–222. <https://doi.org/10.1038/s41370-022-00409-w>.
- Kereszturi, G., Schaefer, L.N., Schleiffarth, W.K., Procter, J., Pullanagari, R.R., Mead, S., Kennedy, B., 2018. Integrating airborne hyperspectral imagery and LiDAR for

- volcano mapping and monitoring through image classification. *Int. J. Appl. Earth Obs. Geoinf.* 73, 323–339. <https://doi.org/10.1016/j.jag.2018.07.006>.
- Kirch, W., 2008. Pearson's correlation coefficient. In: Encyclopedia of Public Health. Springer, Dordrecht. [https://doi.org/10.1007/978-1-4020-5614-7\\_2569](https://doi.org/10.1007/978-1-4020-5614-7_2569).
- Kruse, F.A., Lefkoff, A.B., Boardman, J.B., Heidebrecht, K.B., Shapiro, A.T., Barloon, P.J., Goetz, A.F.H., 1993. The Spectral Image Processing System (SIPS) – interactive visualization and analysis of imaging spectrometer data. *Remote Sens. Environ.* 44, 145–163. [https://doi.org/10.1016/0034-4257\(93\)90013-N](https://doi.org/10.1016/0034-4257(93)90013-N).
- LaRue, M.A., Lynch, H.J., Lyver, P.O.B., Barton, K., Ainley, D.G., Pollard, A., Fraser, W.R., Ballard, G., 2014. A method for estimating colony sizes of Adélie penguins using remote sensing imagery. *Polar Biol.* 37, 507–517. <https://doi.org/10.1007/s00300-014-1451-8>.
- Leppe, M., Michea, W., Muñoz, C., Palma-Heldt, S., Fernandoy, F., 2007. Paleobotany of Livingston island: the first report of a cretaceous fossil flora from Hannah point. USGS Open-File Report 2007-1047, Short Research Paper 081. doi: 10.3133/of2007-1047.srp081.
- Lucieer, A., Turner, D., King, D.H., Robinson, S.A., 2014. Using an Unmanned Aerial Vehicle (UAV) to capture micro-topography of antarctic moss beds. *Int. J. Appl. Earth Obs. Geoinf.* 27, 53–62. <https://doi.org/10.1016/j.jag.2013.05.011>.
- Lu, G., Chen, G., Tian, L., Qin, K., Qian, S., 2016. Minimum noise fraction versus principal component analysis as a preprocessing step for hyperspectral imagery denoising. *Can. J. Remote. Sens.* 42, 106–116. <https://doi.org/10.1080/07038992.2016.1160772>.
- Lynch, H.J., Schwaller, M.R., 2014. Mapping the abundance and distribution of adélie penguins using landsat-7: first steps towards an integrated multi-sensor pipeline for tracking populations at the continental scale. *PLoS One.* 9, e113301.
- Malenovský, Z., Lucieer, A., King, D.H., Turnbull, J.D., 2017. Unmanned aircraft system advances: health mapping of fragile polar vegetation. *Methods Ecol. Evol.* 8, 1842–1857. <https://doi.org/10.1111/210X.12833>.
- Miloš, B., Josef, H., Jana, M., Katerina, S., Alcia, K., 2018. Dehydration-induced changes in spectral reflectance indices and chlorophyll fluorescence of Antarctic lichens with different thallus color and intrathalline photobiont. *Acta Physiol. Plant.* 40, 177. <https://doi.org/10.1007/s11738-018-2751-3>.
- Miranda, V., Pina, P., Heleno, S., Vieira, G., Mora, C., Schaefer, C.E.G.R., 2020. Monitoring recent changes of vegetation in fildes peninsula (King George Island, Antarctica) through satellite imagery guided by UAV surveys. *Sci. Total Environ.* 704, 135295. <https://doi.org/10.1016/j.scitotenv.2019.135295>.
- Mishra, P., Singh, U., Pandey, C.M., Mishra, P., Pandey, G., 2019. Application of student's t-test, analysis of variance, and covariance. *Ann. Card. Anaesth.* 22 (4), 407–411. [https://doi.org/10.4103/aca.ACA\\_94\\_19](https://doi.org/10.4103/aca.ACA_94_19).
- Murray, H., Lucieer, A., Williams, R., 2010. Texture-based classification of sub-Antarctic vegetation communities on Heard Island. *Int. J. Appl. Earth Obs. Geoinf.* 12, 138–149. <https://doi.org/10.1016/j.jag.2010.01.006>.
- Mustafa, O., Esefeld, J., Gramer, H., Maercker, J., Rummel, M.C., Pfeifer, C., 2017. Monitoring penguin colonies in the Antarctic Using Remote Sensing Data. In: TEXTE 30/2017 Environmental Research of the Federal Ministry for the Environment, Nature Conservation, Building and Nuclear Safety (Jena, Germany), Dessau-Roßlau, Germany: Umweltbundesamt, vol. 163, pp. 1862–4804.
- Oloffson, P., Foody, G.M., Herold, M., Stehman, S.V., Woodcock, C.E., Wulder, M.A., 2014. Good practices for estimating area and assessing accuracy of land change. *Remote Sens. Environ.* 148, 42–57. <https://doi.org/10.1016/j.rse.2014.02.015>.
- Pérez-Ortega, S., De los Ríos, A., Crespo, A., Sancho, L.G., 2010. Symbiotic lifestyle and phylogenetic relationships of the biota of Mastodia tessellata (Ascomycota, Incertae Sedis). *Am. J. Bot.* 97, 738–752. doi: 10.3732/ajb.0900323.
- Pfeifer, C., Barbosa, A., Mustafa, O., Peter, H.U., Rümmler, M.C., Brenning, A., 2019. Using fixed-wing UAV for detecting and mapping the distribution and abundance of penguins on the South Shetlands Islands, Antarctica. *Drones.* 3, 39. <https://doi.org/10.3390/drones3020039>.
- Qiao, G., Yuan, X., Florinsky, I., Popov, S., He, Y., Li, H., 2023. Topography reconstruction and evolution analysis of outlet glacier using data from unmanned aerial vehicles in Antarctica. *Int. J. Appl. Earth Obs. Geoinf.* 117, 103186. <https://doi.org/10.1016/j.jag.2023.103186>.
- Rajakumari, S., Mahesh, R., Sarunjith, K.J., Ramesh, R., 2022. Building spectral catalogue for salt marsh vegetation, hyperspectral and multispectral remote sensing. *Reg. Stud. Mar. Sci.* 53, 102435. <https://doi.org/10.1016/j.rsma.2022.102435>.
- Rees, W.G., Brown, J.A., Fretwell, P.T., Trathan, P.N., 2017. What colour is penguin guano? *Antarct. Sci.* 29 (5), 417–425. <https://doi.org/10.1017/S0954102017000190>.
- Rogers, A.D., Frinault, B.A.V., Barnes, D.K.A., Bindoff, N.L., Downie, R., Ducklow, H.W., Friedlaender, A.S., Hart, T., Hill, S.L., Hofmann, E.E., Linse, K., McMahon, C.R., Murphy, E.J., Pakhomov, E.A., Reygondeau, G., Staniland, I.J., Wolf-Gladrow, D.A., Wright, R.M., 2020. Antarctic futures: an assessment of climate-driven changes in ecosystem structure, function, and service provisioning in the southern ocean. *Annu. Rev. Mar. Sci.* 12, 87–120. <https://doi.org/10.1146/annurev-marine-010419-011028>.
- Román, A., Navarro, G., Caballero, I., Tovar-Sánchez, A., 2022. High-spatial resolution UAV multispectral data complementing satellite imagery to characterize a chinstrap penguin colony ecosystem on Deception Island (Antarctica). *Glaci. Remote Sens.* 59 (1), 1159–1176. <https://doi.org/10.1080/15481603.2022.2101702>.
- Rossiter, T., Furey, T., McCarthy, T., Stengel, D.B., 2020. UAV-mounted hyperspectral mapping of intertidal macroalgae. *Estuar. Coast. Shelf Sci.* 242, 106789. <https://doi.org/10.1016/j.ecss.2020.106789>.
- Sáez, P.L., Rivera, B.K., Ramírez, C.F., Vallejos, V., Cavieres, L.A., Corcuera, L.J., Bravo, L.A., 2019. Effects of temperature and water availability on light energy utilization in photosynthetic processes of *Deschampsia antarctica*. *Physiol. Plant.* 165, 511–523. <https://doi.org/10.1111/ppl.12739>.
- Seegers, B.N., Stumpf, R.P., Schaeffer, B.A., Loftin, K.A., Werdell, P.J., 2018. Performance metrics for the assessment of satellite data products: an ocean color case study. *Opt. Exp.* 26 (6), 7404–7422. <https://doi.org/10.1364/OE.26.007404>.
- Shatova, O., Wing, S.R., Gault-Ringold, M., Wing, L., Hoffmann, L.J., 2016. Seabird guano enhances phytoplankton production in the Southern Ocean. *J. Exp. Mar. Biol. Ecol.* 483, 74–87. <https://doi.org/10.1016/j.jembe.2016.07.004>.
- Shatova, O., Wing, S.R., Hoffmann, L.J., Wing, L.C., Gault-Ringold, M., 2017. Phytoplankton community structure is influenced by seabird guano enrichment in the Southern Ocean. *Estuar. Coast. Shelf Sci.* 191, 125–135. <https://doi.org/10.1016/j.ecss.2017.04.021>.
- Shirihai, H., 2003. *The Complete Guide to Antarctic Wildlife*. Princeton University Press, Princeton and Oxford, p. 510.
- Smykla, J., Wolek, J., Barcikowski, A., 2007. Zonation of vegetation related to penguin rookeries on King George Island maritime antarctic. *Arct. Antarct. Alp. Res.* 39 (1), 143–151. <https://doi.org/10.1657/1523-0430>.
- Solhaug, K.A., Gauslaa, Y., 1996. Parietin, a photoprotective secondary product of the lichen *Xanthoria parietina*. *Oecologia* 108, 412–418.
- Sotille, M.E., Bremer, U.F., Vieira, G., Velho, L.F., Petsch, C., Simões, J.C., 2020. Evaluations of UAV and satellite-derived NDVI to map maritime Antarctic vegetation. *Appl. Geogr.* 125, 102322. <https://doi.org/10.1016/j.apgeog.2020.102322>.
- Sparaventi, E., Rodríguez-Romero, A., Barbosa, A., Ramajo, L., Tovar-Sánchez, A., 2021. Trace elements in antarctic penguins and the potential role of guano as source of recycled metals in the southern ocean. *Chemosphere* 285, 131423. <https://doi.org/10.1016/j.chemosphere.2021.131423>.
- Tovar-Sánchez, A., Román, A., Roque-Atienza, D., Navarro, g., 2021. Applications of unmanned aerial vehicles in antarctic environmental research. *Sci. Rep.* 11, 21717. <https://doi.org/10.1038/s41598-021-01228-z>.
- Turner, D., Lucieer, A., Malenovský, Z., King, D., Robinson, S.A., 2018. Assessment of antarctic moss health from multi-sensor UAS imagery with random forest modelling. *Int. J. Appl. Earth Obs. Geoinf.* 68, 168–179. <https://doi.org/10.1016/j.jag.2018.01.004>.
- Van Rossum, G., Drake Jr., F.L., 1995. *Python Reference Manual*. Centrum voor Wiskunde en Informatica, Amsterdam.
- Wang, C., Myint, S.W., 2015. A simplified empirical line method of radiometric calibration for small unmanned aircraft systems-based remote sensing. *IEEE J. Sel. Top. Appl. Earth Obs. Remote Sens.* 8, 1876–1885. <https://doi.org/10.1109/JSTARS.2015.2422716>.
- Wu, J., Xu, W., He, J., Lan, M., 2023. YOLO for penguin detection and counting based on remote sensing images. *Remote Sens.* 15 (10), 2598. <https://doi.org/10.3390/rs15102598>.
- Zmarz, A., Rodzewicz, M., Dąbski, M., Karsznia, I., Korczak-Abshire, M., Chwedzorowska, K.J., 2018. Application of UAV BVLOS remote sensing data for multi-faceted analysis of Antarctic ecosystem. *Remote Sens. Environ.* 217, 375–388. <https://doi.org/10.1016/j.rse.2018.08.031>.